



Investigation of bipolar plate and diffusion media interfacial structure in PEFCs: A fractal geometry approach

Tushar Swamy^a, E.C. Kumbur^b, M.M. Mench^{c,*}

^a Fuel Cell Dynamics and Diagnostics Laboratory, Department of Mechanical and Nuclear Engineering, The Pennsylvania State University, University Park, PA 16802, USA

^b Electrochemical Energy Systems Laboratory, Department of Mechanical Engineering and Mechanics, Drexel University, Philadelphia, PA 19104, USA

^c Fuel Cell Dynamics and Diagnostics Laboratory, Department of Mechanical, Aerospace and Biomedical Engineering, The University of Tennessee, Knoxville, TN 37996, USA

ARTICLE INFO

Article history:

Received 18 October 2010

Received in revised form

17 December 2010

Accepted 20 December 2010

Available online 4 January 2011

Keywords:

Bipolar plate

Contact resistance

Diffusion media

Interface

Polymer electrolyte fuel cell

ABSTRACT

The imperfect interfacial contact between the bipolar plate (BP) and the diffusion medium (DM) can have a significant impact on the multi-phase flow and current transport in an operating polymer electrolyte fuel cell (PEFC). The objective of this work is to describe the impact of the BP and DM surface morphologies and the resulting interfacial contact on PEFC performance. In this study, the surface morphology of several BP and DM samples was digitally characterized using optical profilometry (OP). The benchmark surface data were then utilized in a microscopic model developed to simulate the BP|DM interfacial contact under compression. The microscopic model is based on the fractal modeling approach, which provides an accurate representation of the BP|DM interfacial contact by suppressing the resolution dependence of the surface profiles in consideration. Results indicate that the uncompressed surface morphology of mating materials, elasticity of these components, and local compression pressure are the key parameters that influence the BP|DM contact. The model results show that the void space along the BP|DM interface can potentially store a significant amount of liquid water (from 0.85 to 3.5 mg/cm²), which can result in reduced durability and performance of the PEFC. The model predicts that a 50% drop in the DM surface roughness results in nearly a 40% drop in the BP|DM contact resistance and a 15% drop in the BP|DM interfacial water storage capacity.

© 2010 Elsevier Ltd. All rights reserved.

1. Introduction

Polymer electrolyte fuel cells (PEFCs) have tremendous potential as a power source, which has led to an increased interest in their usage for various applications. However, certain performance limitations have yet to be fully explained for further system optimization [1]. In particular, ohmic and mass transport losses can originate at the various interfaces that exist between the fuel cell components, including between the bipolar plate and the diffusion media (BP|DM). Among the interfaces in PEFC, the BP|DM interface has some important implications on the performance, since this interface significantly contributes to the interfacial contact resistance of the cell (up to ~20% of the total ohmic resistance in a PEFC under certain conditions) [2], and affects the channel liquid water distribution. Despite its importance, little is known or understood regarding the BP|DM interfacial structure and related effects on the performance and durability of PEFCs. Therefore, in order to close this gap in the literature, the main emphasis in this study was

placed on understanding the role of the BP|DM interfacial morphology, applied compression pressure, and material properties of the contacting surfaces on the performance characteristics of a PEFC.

Due to the inherent roughness and morphological structure of the BP and DM surfaces, the contact between the two materials under compression is imperfect (illustrated in Fig. 1), which results in a loss of contact area and the formation of interfacial gaps between these two surfaces. The incomplete contact not only results in an undesirable electronic contact resistance (that typically dominates all other interfacial contact losses in the PEFC), but also can lead to liquid water pooling in the interfacial void space. Water pooling can result in increased water overhead in the fuel cell during operation, making shutdown to a safe frozen state more difficult, and potentially reducing operational performance. Therefore, it is necessary to investigate the impact of the BP|DM interface to further improve the cell design.

There are many modeling studies in the literature that investigate the impact of BP [3–11] and the DM [12–19] on the performance of PEFCs. In general, these modeling studies do not consider a distinct BP|DM interfacial region; instead they apply numerical boundary conditions (*i.e.* flux and concentration matching) at the bordering control volumes of the mating surfaces that

* Corresponding author. Tel.: +1 865 974 5115.

E-mail address: mmench@utk.edu (M.M. Mench).

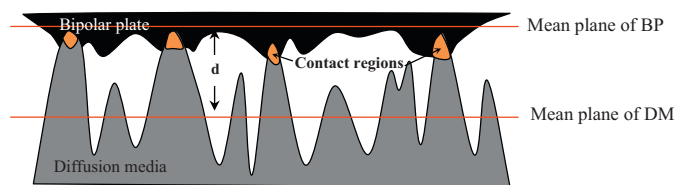


Fig. 1. 2D schematic of the BP|DM interfacial contact (not to scale).

form the interface, ignoring the unique physical characteristics of the interfacial region. Although, there exist a few experimental studies that have focused on BP|DM interfacial losses [20–27], water management issues arising from imperfect contact at the BP|DM interface are not yet definitely explored. Although a few numerical studies have attempted to incorporate the BP|DM interface into the modeling framework [25,28–32], these models neglect the morphological features of the BP and DM surfaces; instead they consider a lumped or macroscale representation of the resulting interface. A few studies have attempted to model the BP|DM interfacial contact resistance in a PEFC [23,33–36], some of which take the average or a generic representation of the morphology of the mating surfaces into consideration [23,33,35]. However, to the best of the authors' knowledge, the characteristics of the actual BP|DM interfacial morphology and related effects on the performance of PEFCs are yet to be fully explored.

Although interfacial modeling has been scarcely dealt with in PEFCs [12,23,33–41], contact models have been extensively developed and studied in the field of tribology and electrical contact mechanics [41–53]. To date, the most common approach to simulate the interfacial contact is based on the Hertzian theory of contact and probabilistic modeling techniques, which can account for the stochastic nature of the mating surface profiles [41–46]. These techniques can represent the surface roughness characteristics of the contacting surfaces by utilizing characteristic stochastic parameters that are extracted from measured variance of heights, slope and the curvature of the surface profiles. Since these geometric parameters are dependent on the resolution of the roughness measurements, these approaches can be employed in cases where the root mean square (RMS) roughness of the contacting surfaces are proportional to the sampling interval of the measuring instrument [37]. However, for the cases where the roughness metrics are sensitive to the adopted sampling interval of the measuring instrument (such as in the PEFCs, where the average RMS roughness of the DM ($\sim 25.2 \mu\text{m}$) is much greater than the sampling interval of the surface measurements), a fractal geometry based approach is needed to describe the nature of the rough surfaces that are in contact [47–53]. Since the fractal contact approach is independent of the sampling interval of the measuring instrument, and depends only on the surface profiles and material properties, it can be extended to simulate the BP|DM interfacial contact in PEFCs, once the reliable surface profile statistics are obtained, and the necessary model approximations are justified.

This study is motivated by the need to gain a better understanding of the BP|DM interfacial contact characteristics by considering the actual BP and DM surface morphology and mating characteristics. The specific objective is to characterize the BP and DM interfacial morphology, followed by the development of a fractal contact based analytical model to predict the BP|DM contact resistance and the potential water accumulation capacity of the BP|DM interface under compression. The model is also capable of digitally reconstructing the BP|DM interfacial morphology via control volume allocation, which can be further incorporated into a macroscopic fuel cell model to enable a more accurate quantification of the governing losses and the PEFC performance.

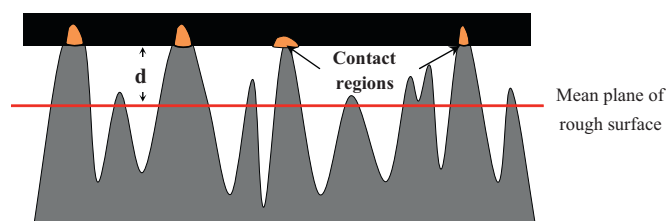


Fig. 2. Schematic of mean separation, d , and contact regions for a smooth and rough surface contact.

2. Method of approach

The key input parameters required for the BP|DM interface model presented herein are a function of the BP and DM surface profile characteristics [51]. These parameters can be evaluated if the discrete surface profile data of the two surfaces are known [51]. For this purpose, optical profilometry was used to obtain the BP and DM surface profile data. A description of the measurement technique is given in the following section, followed by the interface model formulation presented in this study.

2.1. Experimental

The surfaces of graphite and metal bipolar plate, and a widely used carbon paper based fuel cell DM (SGL 10BB) were subjected to investigation to generate the datasets regarding the surface profile characteristics of these materials. It was observed that the surface of the tested DM samples exhibit higher roughness than the graphite BP. Among the BPs, the metal plate was observed to have a smoother surface than graphite plate, indicating that the metal BP is expected to have a relatively smaller effect on the BP|DM interfacial structure as illustrated in Fig. 2. Therefore, the discussion on the metal BP|DM interface is omitted, and the main emphasis in this study is placed on the graphite BP|DM interface.

In this study, optical profilometry was used as an imaging technique to quantify the surface roughness and capture the morphological features of these samples. The key advantage of this technique is that it can perform non-contact, high vertical resolution and quantitative measurements of a broad range of areas within the tested sample [54]. Optical profilometry measurements were performed using a Wyko NT100 optical profilometer in VSI mode. The resolution in z -direction was approximately 3 nm, and the scanned areas were $598 \mu\text{m} \times 454 \mu\text{m}$ in size with a sampling interval of $0.82 \mu\text{m}$ in the x -direction and $0.95 \mu\text{m}$ in the y -direction.

In order to accurately capture the surface characteristics by optical profilometry, surfaces of interest should possess a high degree of reflectivity. Based on our prior experience, the carbon based DM surfaces possess low reflectivity, having light dispersive characteristics, which can limit data acquisition [38]. Therefore, for improved image acquisition, DM samples were sputtered with a thin layer of gold (Au) to enhance the reflectivity of the scanned surfaces for high resolution quantification of the surface perturbations of the tested samples. It is important that the sputtered gold layer thickness be optimized to avoid any possible significant alteration of the surface patterns due to the sputtering process [54,55]. A special measurement procedure consisting of two steps was designed to determine the optimum sputtering thickness that is required to perform optical profilometry measurements on the DM surface. In Step 1, the DM samples, which were sputtered for different amounts of time, were scanned using optical profilometry. Thereafter, the images obtained were compared to quantify the change of surface reflectivity of the DM sample as a function of sputtering time in order to determine the optimum sputtering time for optical profilometry

measurements. In Step 2, special screening protocols were performed by SEM imaging analysis to quantify the change of surface patterns (*i.e.* particle growth, roughness) as a function of sputtering time and thickness. Due to the varying nature of surface topology, the changes in DM surface morphology with sputtering can only be determined by examining the exact same region on the sample surfaces before and after sputtering. Since optical profilometry does not satisfactorily allow for isolated measurement of targeted regions, the SEM images of the sputtered regions on the specimen surfaces were compared with the virgin case to quantify possible changes in the topological features of the sputtered surface. After all these analyses, the optimum sputtering time that yields sufficiently dense quantitative profilometry data with minimal changes in the surface morphology was determined. For the tested DM samples, the sputtering times less than or equal to 6 min was observed to yield a dense matrix of profilometry data with no significant changes in the measured surface patterns.

Although in this work, the data only for the carbon paper type DM is presented, it must be noted that the model described is capable of simulating the BP|DM interface of other DM materials (*e.g.* cloth or felt) with comparable accuracy, given comparable input data of surface morphology and material properties. Therefore, the data presented are applicable for the type of paper DM chosen only. Paper material characteristics were chosen since this material is the most widely used in PEMFCs.

2.2. Model formulation

The BP|DM interface model presented herein requires two key input parameters, the fractal dimension, D , and the topothesy, G (scaling constant), which are directly related to the BP and DM surface profile characteristics [51]. The parameters D and G are scale independent, therefore can accurately represent the BP|DM interfacial morphology. The term D can take any value between 1 and 2, where a smaller value represents a smoother profile, implying that the low frequency components are dominant in amplitude. As D is increased, the high frequency components of surface data become comparable in amplitude with the low frequency ones [51]. The topothesy, G , determines the amplitude of roughness on the surface with larger values corresponding to higher degree of roughness [51]. The discrete surface data from optical profilometry measurements were first processed to evaluate these fractal morphological parameters (D and G) of the BP and DM interface. These BP and DM fractal parameters were then implemented into the elastic–plastic BP|DM interface model in order to obtain the mean separation distance between the contacting BP and DM surfaces [52], which was used to determine the BP|DM contact resistance [53]. In general, the model formulation is divided into the following steps: (a) surface profile characterization; (b) elastic–plastic regime of contact spots; (c) size distribution of contact spots; (d) surface separation calculation; (e) contact resistance calculation. Formulation of the model steps are provided in Appendix B. The reader is encouraged to refer to Refs. [51–53] for a detailed description of the model formulation. The model results are discussed in the following section.

3. Results and discussion

3.1. Experimental results

Optical profilometry results indicate that both BP and DM surfaces exhibit a high degree of roughness, having structures such as high hills, large valleys as shown in Figs. 2 and 3. Table 1 provides a set of three roughness parameters that were used to compare the surface roughness of BP and DM surfaces. Specific roughness parameters (λ_a , λ_q and λ_t that are described in detail in [56]) gath-

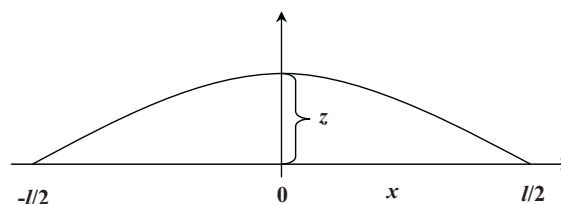


Fig. 3. Geometry of a contact spot of length scale l .

ered from optical profilometry measurements, suggest that DM surface exhibits a relatively higher degree of roughness compared to BP surface (Table 1), indicating that the stiffness and the uncompressed roughness of the DM are the two key parameters that control the interfacial contact characteristics at the BP|DM interface.

Optical profilometry images of the BP and DM also suggest that there are significant differences between in Figs. 4 and 5. The surface morphological features of the BP and DM in terms of their orientation, size, shape and depth, as shown in Figs. 4 and 5. Fig. 4 clearly highlights the constituent fiber matrix in the DM materials (that has randomly oriented fibers), which is responsible for the observed contours on the surface of the DM. It is very likely that the existence of the randomly oriented fiber matrix on DM surface results in large void regions and irregular surface perturbations (Fig. 4), yielding relatively high degree of surface roughness patterns, as indicated by the roughness metrics given in Table 1. The presence of large void regions indicates the existence of possible water accumulation sites at the BP|DM interfaces. While the DM exhibits considerable surface roughness, Fig. 5 indicates that the graphite BP surface contains regions of different roughness values distinctly separated from each other. However, the BP is observed to experience a relatively smoother surface, where the measured surface perturbation seems to follow a more homogeneous trend, as also suggested by the roughness metrics in Table 1. The existence of these distinct regions can be attributed to the machining process employed during fabrication of these BP materials.

3.2. Model results

Prior to conducting a parametric study of the BP|DM interface, a verification study was conducted to determine if the present model, adopted from [52], was implemented correctly. A parametric study was performed in [52] to demonstrate the relation between non-dimensional contact area and load. The same study is repeated using the current model for comparison, where the variation of the dimensionless contact area versus the dimensionless load (Fig. 6) for a different contact problem given in [52], were simulated. Fig. 6 shows a comparison between the model results in literature and the current model predictions for the case given in [52]. The results from the current model and reported model predictions in [52] show excellent agreement, indicating that the present model can successfully simulate the resulting contact interface between the two materials in consideration.

Reverting back to the BP|DM contact, the D and G values obtained for the BP|DM interface are provided in Table 2. Fig. 7 depicts

Table 1
Measured surface roughness data of BP and DM samples (arithmetic mean values \pm standard deviation of measurements).

Sample	Mean roughness, λ_m (μm)	RMS roughness, λ_q (μm)	Crest-trough roughness, λ_t (μm)
BP	1.38 ± 1.12	1.64 ± 0.84	14.36 ± 1.43
DM	19.65 ± 2.15	25.21 ± 1.43	161.56 ± 23.54

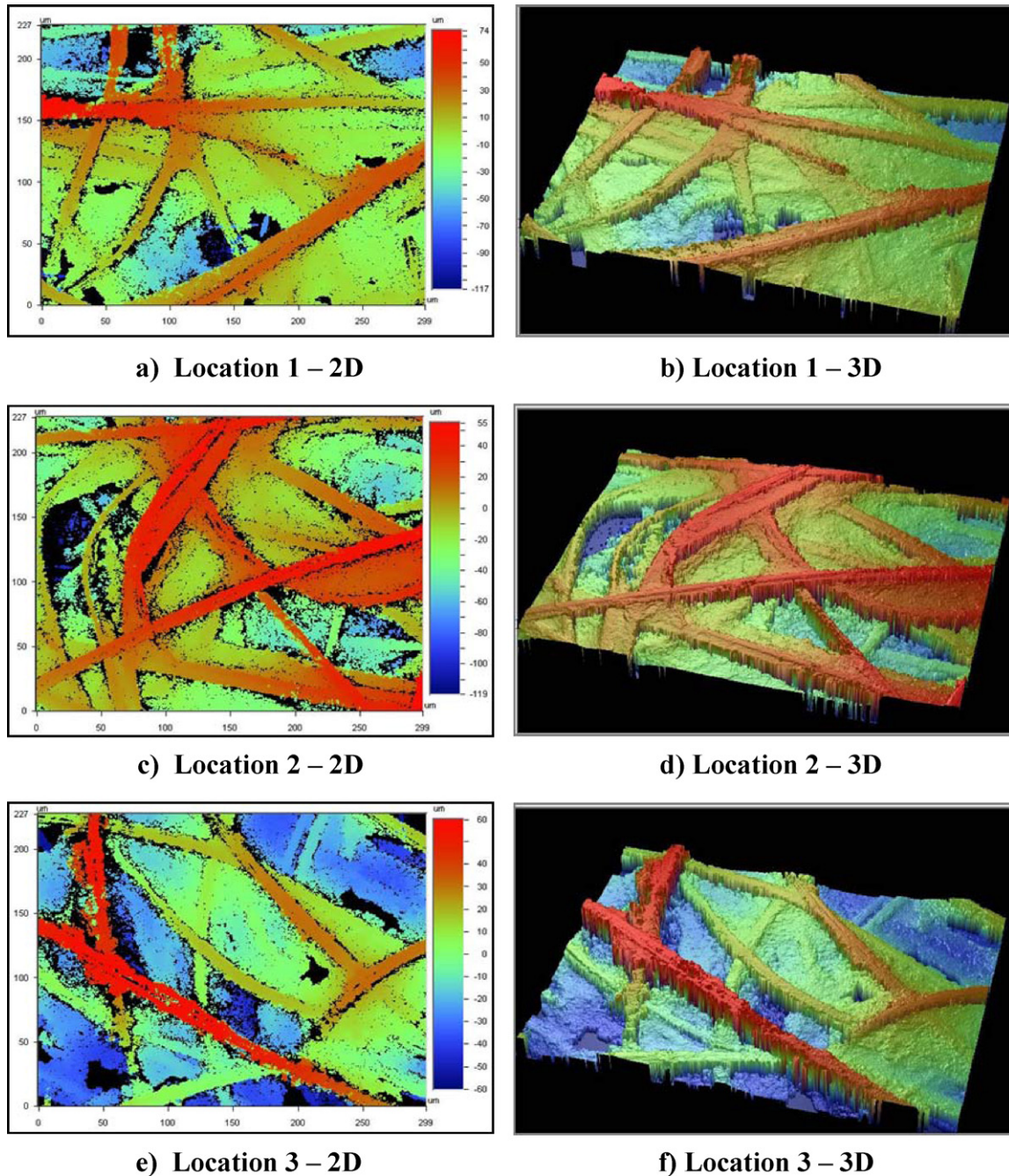


Fig. 4. 2D and 3D optical profilometry images of SGL 10BB DM surface at various locations.

Table 2

Average and location specific fractal parameter values of the BP|DM interface.

Location	D (unitless)	G (μm)
1	1.58	2.42
2	1.64	2.61
3	1.71	2.54
4	1.59	2.23
5	1.86	2.59
6	1.79	2.47
7	1.82	2.29
8	1.77	2.38
9	1.83	2.51
10	1.71	2.46
Average	1.73	2.45

the variation of the BP|DM contact resistance as a function of the applied compression pressure in a PEFC. A comparison of the current model prediction with the data reported in [23] is also presented in Fig. 7. A comparison between the results is warranted since the experiments performed by the authors of Ref. [23] used SGL-10BB DM and XM9612 graphite BP as the interfacing components. The authors of Ref. [23] performed interfacial contact resistance measurements using a Tetrahedron MTP-10 press to provide a series of prescribed clamping pressures, and a Quadtech 1880 milliohm meter to measure the electrical resistance. The DM layer was sandwiched between two BPs, and this assembly was placed between two gold plates. The total system resistance was calculated, and knowing the bulk resistances of the materials and the BP|Au contact resistance [23], the BP|DM interfacial resistance value was extracted. Fig. 7 clearly shows that the current model pre-

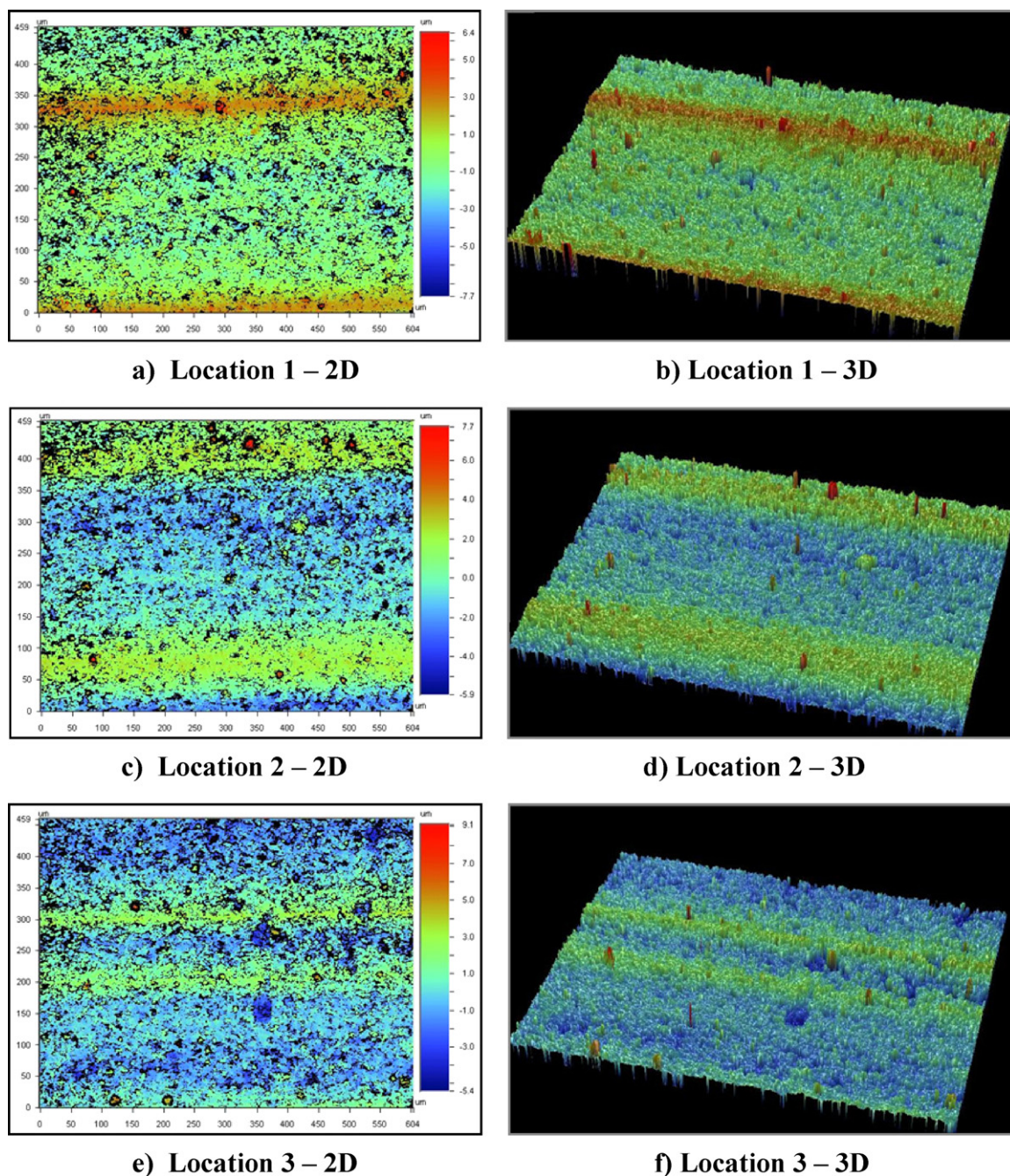


Fig. 5. 2D and 3D optical profilometry images of graphite BP surface at various locations.

dictions and the experimental/model results from [23] are in good agreement. Fig. 7 indicates that the BP|DM contact resistance is significantly high under a compression pressure of 1.5 MPa, which typically exists inside the cell. This observation can be attributed to the fact that due to the highly rough nature of the DM surface, a relatively small number of asperities located on the DM surface come into contact with the asperities on the BP surface at nominal pressure. The decrease in amount of contact points can impede the electron flow across the interface, thereby resulting in an increased BP|DM interfacial resistance.

Fig. 8 shows the virtually-cloned BP|DM interfacial structure under homogeneous compression of 1.5 MPa (e.g. under a land). The virtual interface structure shown in Fig. 8 clearly depicts the morphological features of the two contacting surfaces, demonstrating the relatively smoother nature of the BP surface as compared to

the DM surface. The virtual interface (Fig. 8) also shows the existence of large interfacial gaps and some deep cracks, which most likely originate from the highly rough nature of DM surface and heterogeneous fiber matrix constituent within the DM material. The separation between mean planes, d , was determined to lie in the range of 15–20 μm . The maximum gap width was found to be close to 30 μm . It is evident from Fig. 8 that the BP|DM interfacial gaps are relatively larger in dimension as compared to the average pore size in the DM layer, which supports the results reported in [1]. This observation suggests that the BP|DM interface can act as a locally low capillary pressure region, which can store significant amount of liquid water (e.g. especially under landings, as observed in neutron imaging studies [60–62]). The material properties of the BP and DM materials used in this work are listed in Table 3.

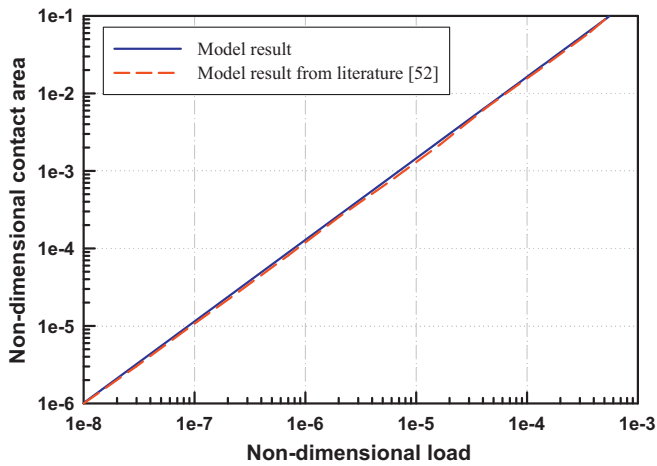


Fig. 6. Verification plot of non-dimensional area of contact versus the applied non-dimensional load, comparing current model results with the data reported in literature [52].

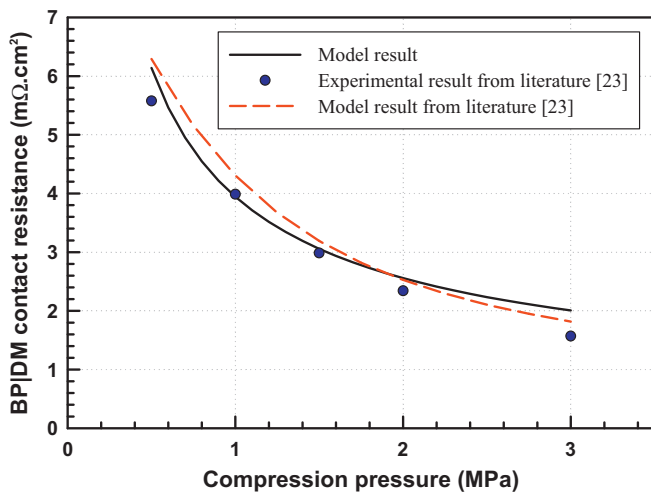


Fig. 7. Predicted BP|DM contact resistance (CR) versus applied compression pressure. Experimental and model results from literature [23] are compared.

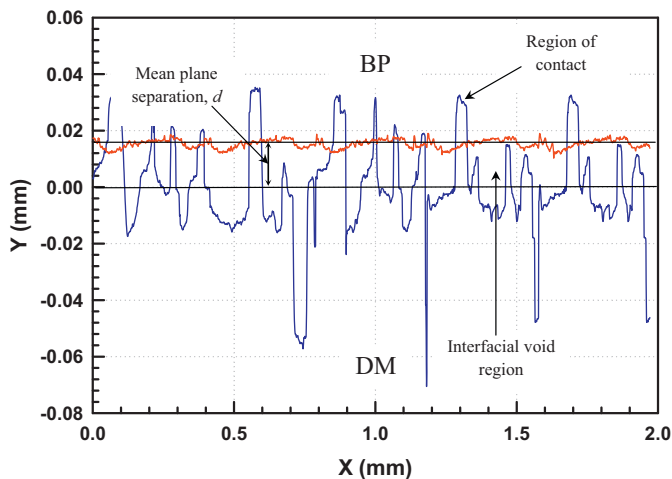


Fig. 8. Virtually created BP|DM interface structure using present model.

Table 3

Material properties of the contacting surfaces.

Properties	Material	Value	Units	Reference
Young's modulus	DM	10,000	MPa	[57]
Young's modulus	BP	10,000	MPa	[57]
Electrical conductivity (through plane)	DM	300	S m ⁻¹	[58]
Electrical conductivity (through plane)	BP	20,000	S m ⁻¹	[58]

Fig. 9 shows the predicted variation of the BP|DM contact resistance as a function of the applied compression pressure for different degrees of DM surface roughness. It should be noted that since the DM surface exhibits a higher degree of roughness as compared to the BP surface, the surface characteristics of the DM is expected to dominate the interfacial region, and consequently the BP|DM contact resistance. It can be seen from Fig. 9 that lowering the roughness of the DM surface by 50% (i.e. reducing the topography of the DM by 50%) results in nearly a 40% drop in the BP|DM interfacial resistance. This significant drop in the contact resistance can be attributed to the fact that as the roughness of the mating surfaces is reduced (i.e. smoother contact), the number of contact points at the interface increases, which in turn, facilitates the electron flow across the BP|DM interface. A similar result is also expected for thermal contact resistance within this interfacial region.

Fig. 10 shows that the impact of the variation of Young's modulus of the DM and BP surfaces on the BP|DM contact resistance for a homogeneous compression pressure of 1.5 MPa (a typical compression under the land). It is observed that a 50% drop in the Young's modulus of the DM and BP yields approximately a 38% drop in BP|DM contact resistance. The strong dependence of the contact resistance on the Young's modulus of the interfacing materials can be attributed to the fact that a drop in the Young's modulus of the DM and BP surfaces results in the softening of these materials, enabling the surfaces to exhibit a higher degree of conformation under compression. The increased conformation of these layers enhances the local interfacing percentage. As a result, a higher number of asperities come into contact, and the BP|DM contact resistance is lowered, as predicted by the present model (Fig. 10).

Utilizing the mean plane separation, d (obtained as a model output), and the BP|DM surface profile information, the capacity of potential water accumulation (i.e. interfacial water storage capacity) in the BP|DM interfacial gaps can be predicted. Quantification of the maximum water content in the BP|DM interface with respect to the total amount of water in a PEFC is critical as it allows us to

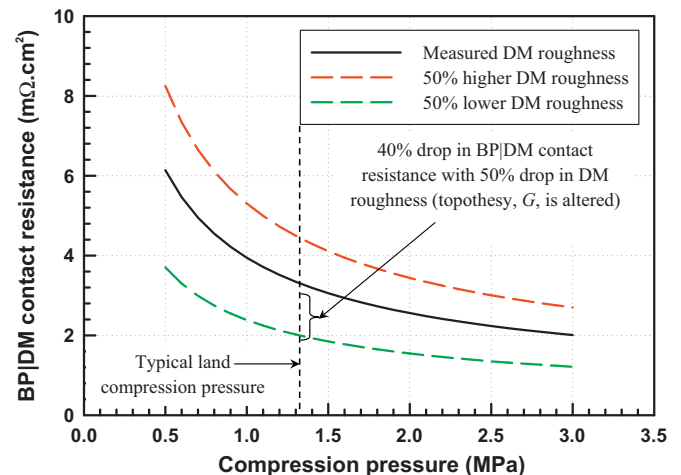


Fig. 9. Predicted BP|DM contact resistance versus compression pressure for different degrees of DM roughness.

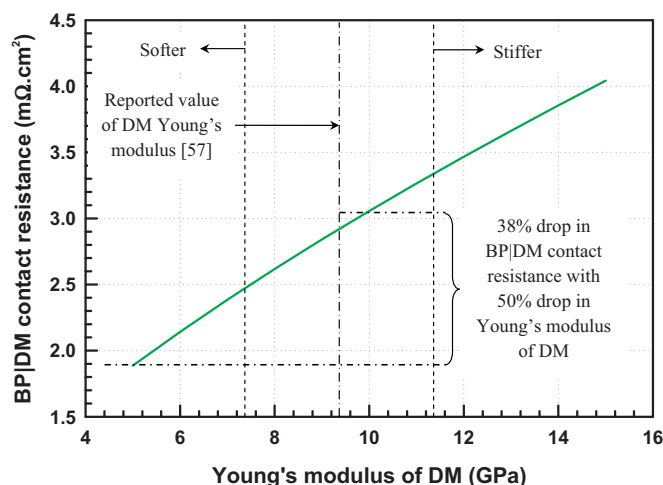


Fig. 10. Effect of the Young's modulus of the DM layer on the predicted BP|DM contact resistance for homogeneous compression pressure of 1.5 MPa (under a typical land).

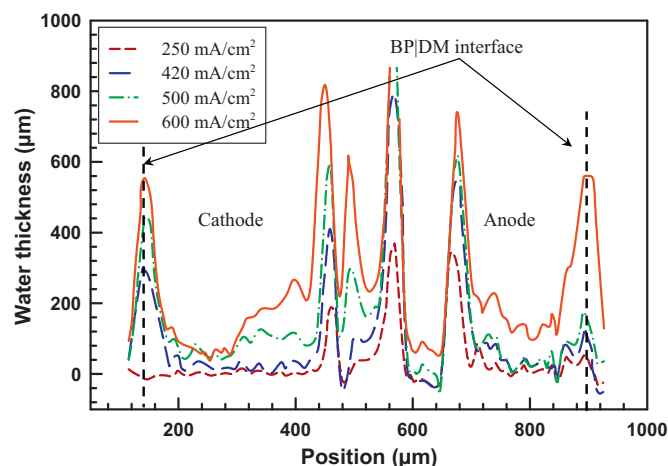


Fig. 12. Experimental quantification of liquid water distribution in a PEFC via X-ray imaging, showing significant water storage at the BP|DM interface (Figure adapted from [63]).

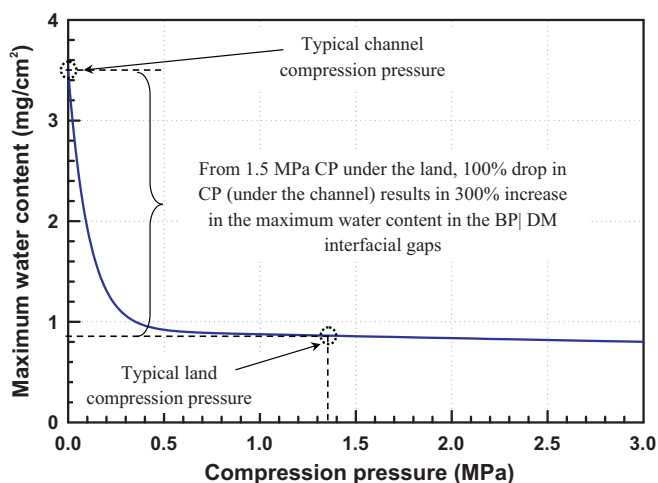


Fig. 11. Effect of the compression pressure (CP) on the maximum stored water content in the BP|DM interfacial gaps.

qualitatively estimate the impact of the BP|DM interfacial structure on the mass transport losses. Fig. 11 shows the variation of the predicted maximum water content in the BP|DM interface as a function of the applied assembly compression pressure. Fig. 11 indicates that the BP|DM interface can hold approximately 0.85–3.5 mg/cm² of liquid water when fully filled. The lower and upper limits of the prediction are at homogeneous compression pressures of 1.5 MPa (*i.e.* under the land condition) and 0.0001 MPa (≈ 0 MPa, *i.e.* under the channel where no interface exists), respectively. Recent neutron imaging results [59–62] suggest that nearly 5–15 mg/cm² of water can be stored in a PEFC under normal operating conditions. Comparing neutron imaging data and current model predictions, it is estimated that the BP|DM interface can store nearly 5–16% of the total water content in the PEFC, which is significant considering the overall water balance in PEFCs. In addition, cross-sectional X-ray radiography results [63] (shown in Fig. 12) supports this finding, suggesting that the BP|DM interface can store a considerable amount of liquid water (550 μ m water thickness at 600 mA/cm²) due to the interfacial gaps at the interface. As it has been shown in recent neutron imaging studies that water tends to accumulate under lands, minimizing the interfacial gaps via more smooth contact at the BP|DM interface would be one potential solution to reduce excess liquid water storage in PEFCs. It must be noted

that the water storage estimation provided in the article would be affected if post compression morphology of the contacting layers was used as input. However, it is argued that it is only at the contact spots where the post compression roughness of the layers would experience a change. In addition, to further investigate this issue, special experiments were performed at different compression to gauge the effects of compression on the surface roughness characteristics of carbon paper diffusion media. Optical profilometry scans showed negligible change in the surface roughness characteristics of the DM in response to different compression loadings, indicating that compression appears to have minor effect; therefore the morphology of the layers at the void regions would incur minor changes. Therefore, it is pointed out that although the post compression morphology data is necessary to more accurately predict interfacial water content, the change in the interfacial void volume is expected to be relatively small, and may not greatly affect the water storage values estimated by the present model.

In terms of compression, the current model predictions suggest that an approximate 100% drop in the compression pressure results in nearly a 300% increase in the maximum water content in the BP|DM interfacial gaps (Fig. 11). This suggests that the local compression pressure in a fuel cell has a significant impact on the maximum potential water content that can be stored in the BP|DM interface. It is not suggested here that the entire BP|DM interfacial void volume is indeed normally filled with liquid water; instead, the present model predictions underline the existence of a significant potential storage location along the BP|DM interface, which can potentially be reduced through further engineering.

Fig. 13 shows the predicted impact of the DM surface roughness on the maximum water content in the BP|DM interfacial gaps. It is estimated that a 50% drop in DM (same method in Fig. 9 is adopted here to achieve the drop in roughness) yields nearly a 15% drop in the maximum water content at a compression pressure of 1.5 MPa (*i.e.* under landings). The predicted drop in maximum water content may be attributed to the drop in interfacial void volume due to the decrease in DM surface roughness.

4. Summary and conclusions

A fractal geometry model was developed to investigate the effect of the BP and DM surface morphology and the applied compression pressure on the ohmic and mass transport losses at the BP|DM interface in a PEFC. Results show that the roughness of the DM surface

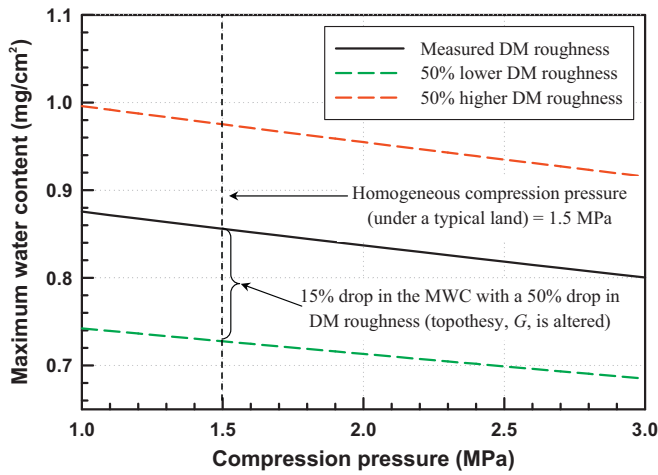


Fig. 13. Effects of the variation in DM surface roughness on the maximum water content (MWC) in the BP|DM interfacial voids for a range of applied compression pressures.

and the elastic modulus of the interfacing materials have a significant impact on the polarization losses associated with the BP|DM interface. The main conclusions are summarized below:

- (1) The results indicate that the DM surface tends to exhibit much higher roughness as compared to the BP surface. Therefore, it is more beneficial to tailor the DM surface morphology to improve contact at the BP|DM interface.
- (2) The BP|DM interface contains large interfacial gaps, which can result in significant water pooling at this interface. The model suggests that the BP|DM interfacial voids can hold approximately 5–16% of the total liquid water content observed in the PEFC during operation.
- (3) For a homogeneous compression pressure of 1.5 MPa (i.e. under a typical land), a 50% drop in the Young's modulus of the DM was predicted to yield a 38% drop in the BP|DM interfacial resistance. In addition, a 50% drop in the DM surface roughness results in a 40% drop in the BP|DM contact resistance and a 15% reduction in the potential water storage capacity of the BP|DM interfacial gaps.
- (4) Results indicate that a softer DM would perform better under the land, maintaining better interfacial contact; however, a stiffer DM may be favored under the channel, as it can counteract the drop in the compression pressure on the DM surface, minimizing the DM intrusion to the flow channel to reduce the pressure drop in the flow channel.

Acknowledgements

The authors would like to thank Dr. Liming Chang, Professor of Mechanical Engineering at The Pennsylvania State University for providing useful insight and support in developing the interface model. The authors would also like to thank F.E. Hızir for optical profilometry measurements, roughness analysis and other valuable discussions on the analysis of some of the results.

Appendix A. Nomenclature

z	height of asperity (μm)
G	topothesy (μm)
D	fractal dimension
L	characteristic length scale (μm)
ω	spatial frequency (μm^{-1})

A	contact area (μm^2)
R	radius of curvature (μm)
H	hardness (MPa)
Y	yield strength (MPa)
E_i	Young's modulus ($i = 1, 2$) (MPa)
ν_i	Poisson's ratio ($i = 1, 2$)
P	compression load (kg)
s	size distribution of contact spots
p	compression pressure (MPa)
σ	standard deviation (μm)
d	surface mean plane separation (μm)
ρ	average resistivity ($\Omega \mu\text{m}$)
R	resistance ($\text{m}\Omega \text{cm}^2$)
λ	roughness (μm)

Subscripts

r	real
l	largest
s	smallest
c	critical
e	elastic
p	plastic
a	apparent
m	mean
q	root mean square
t	maximum height of the surface

Superscripts

$*$	dimensionless
-----	---------------

Appendix B.

The steps of the model formulation as mentioned in Section 2.2 are described here on.

B.1. Surface profile characterization

The BP and DM surface profiles are modeled as a fractal profile using the Weierstrass–Mandelbrot (W–M) function as described in [51]:

$$z(x) = G^{D-1} \sum_{n=n_1}^{\infty} \frac{\cos(2\pi\gamma^n x)}{\gamma^{(2-D)n}} \quad (1)$$

There are three unknown parameters in Eq. (1) which are the topothesy, G , the fractal dimension, D , and n_1 . The value γ is a constant which determines the frequency spectrum of the surface roughness. An initial value of $\gamma = 1.5$ was chosen to provide phase randomization and high spectral density [51]. The lowest frequency in the frequency spectrum is related to the characteristic length (L) of the sample, which can be described as [51]:

$$\gamma^{n_1} = \frac{1}{L} \quad (2)$$

whereas the discrete W–M power spectrum can be approximated as [51]:

$$S(\omega) = \frac{G^{2(D-1)}}{2 \ln(\gamma)} \frac{1}{\omega^{(5-2D)}} \quad (3)$$

In order to find the proper G and D values of the interface, the power spectrum of the BP and DM surface profiles was compared to the power spectrum equation in Eq. (3). The average slope of the W–M power spectrum on a log plot was taken as the fractal dimension (D), whereas the topothesy (G) is the intercept of the W–M power spectrum on the power axis [51]. The D and G values of the BP and DM surfaces at ten different locations were evaluated

using the measured roughness datasets that correspond to each region, and the statically averaged values of these parameters for the two surfaces were used as the D and G values for the BP|DM interface (Table 2).

B.2. Elastic–plastic regime of contact spots

The roughness of the BP and DM surfaces is approximated to be statistically isotropic and the interactions between neighboring asperities are assumed to be negligible. Additionally, the work hardening due to plastic–elastic transition, variation of material hardness with depth from the surface, and the frictional forces between deforming asperities are considered to be negligible. Moreover, the radius of curvature depends on the size of contact, and therefore is incorporated in the fractal model.

Eq. (4) below represents the relation between the roughness amplitude, δ , and the length scale, l , which can be obtained from the W–M function for a single frequency mode of $\gamma^n = 1/l$. For this case, the roughness amplitude (δ) can be correlated to the sample length (l), as [52]:

$$\delta = G^{D-1} l^{2-D} \quad (4)$$

Consider the interface between a statistically isotropic rough surface and a smooth plane (Fig. 2), where the contact spots are of different sizes, and distributed randomly over the contact interface. Let the size-distribution of contact spots be $n(a)$, such that $n(a)da$ is equal to the number of contact spots of area between a and $a+da$. Then the actual area of contact, A_r , can be correlated to $n(a)$ as follows [52]:

$$A_r = \int_{a_s}^{a_l} n(a)ada \quad (5)$$

where, a_l and a_s are the area of the largest and smallest spots, respectively ($a_s = 0$).

Now consider one spot of area a , and the characteristic length scale $l = a^{1/2}$ (it is approximated that the contact spot is circular). The idea behind the fractal model is to first determine the contact spot area a , then predict the deformation required to obtain that spot area from Eq. (4), and finally predict the load required for such a deformation. For a given contact spot of area a , the height of deformation can be calculated from $\delta = G^{D-1} a^{1-D}/2$. The spectrum suggests that the roughness is composed of sinusoidal waves of different wavelengths and amplitudes superimposed on each other. From the W–M function, it is clear that for a wavelength of $l = \lambda^n$, the roughness is a co-sinusoidal wave for which the asperity shape before deformation can be described as (Fig. 3) [52]:

$$z(x) = G^{D-1} l^{2-D} \cos\left(\frac{\pi x}{l}\right); \quad -\frac{l}{2} < x < \frac{l}{2} \quad (6)$$

The radius of curvature, R , at the tip of the asperity is given by [52]:

$$R = \left| \frac{1}{d^2 z / dx^2} \right|_{x=0} = \frac{l^D}{(\pi^2) G^{D-1}} = \frac{a^{D/2}}{(\pi^2) G^{D-1}} \quad (7)$$

Depending on the radius of curvature, R , and the deformation, δ , the contact spot will be either in elastic or plastic deformation. The critical deformation, δ_c , for the inception of plastic contact of a hemisphere can be shown as [52]:

$$\delta_c = \left(\frac{\pi KY}{2E} \right)^2 R \quad (8)$$

where Y is the yield strength of the softer material, and E , is the composite elastic modulus, which can be represented as a function

of Poisson's ratio (ν) [52].

$$E = \left[\frac{1 - \nu_1^2}{E_1} + 1 \frac{1 - \nu_2^2}{E_2} \right]^{-1} \quad (9)$$

The yield strength Y can be expressed as a function of hardness (H) and an arbitrary coefficient K [52]:

$$H = KY \quad (10)$$

Substituting Eq. (7) into Eq. (8) gives:

$$\delta_c = \left(\frac{K\phi}{2} \right)^2 \frac{a^{D/2}}{G^{D-1}} \quad (11)$$

where $\phi = Y/E$ is a material property. If $\delta > \delta_c$, then the asperity is in plastic contact. Using Eq. (4) and Eq. (8), it is found that for a contact spot of area a to be in plastic deformation, it should satisfy the relation $a < a_c$, where a_c is the critical area demarcating the elastic and plastic regimes, and is obtained by equating δ and δ_c [52]:

$$a_c = \frac{G^2}{(K\phi/2)^{2/(D-1)}} \quad (12)$$

This suggests that small contact spots lie in the region of plastic deformation, whereas the large contact spots are in elastic contact. The reason for the less deformation for a small contact spot can be explained by the fact that the small area of contact (Eq. (7)) yields small radius of curvature, which results in a lower value of the critical deformation δ_c . Since both R and δ_c vary with $a^{D/2}$, and δ varies as $a^{(2-D)/2}$, the condition of $\delta > \delta_c$ can be satisfied only by smaller contact spots of area $a < a_c$ [52]. On the other hand, if the contact spot area is greater than the critical area ($a > a_c$) then the spot can be considered in elastic deformation region, and therefore the relation between the area, deformation (δ) and the elastic load, P_e can be described by the Hertzian theory as [52]:

$$a = \pi R \delta \quad (13)$$

$$P_e(\delta) = \frac{4}{3} ER^{1/2} \delta^{3/2} \quad (14)$$

Substituting δ and R in Eq. (14) from Eqs. (13) and (7) gives us [52]:

$$p_e(\delta) = \frac{4\sqrt{\pi} EG^{D-1} \delta^{(3-D)/2}}{3} \quad (15)$$

If the contact spot is in plastic deformation (that is if it satisfies $a < a_c$), then the load on the spot can be given as [52]:

$$P_p(a) = KYa \quad (16)$$

Combining Eqs. (15) and (16), the total load on the surface can be evaluated using the size distribution of contact spots, $s(a)$. If the largest contact spot has an area greater than the critical area (that is $a_l > a_c$), then the total load can be given as [52]:

$$P = \frac{4\sqrt{\pi} EG^{D-1}}{3} \int_{a_c}^{a_l} s(a) a^{(3-D)/2} da + KY \int_{a_s}^{a_c} s(a) ada \quad (17)$$

For the case of $a_l < a_c$ where all the contact spots are in plastic contact, the total load can be written as [52]:

$$P = KY \int_{a_s}^{a_l} s(a) ada = KYA_r \quad (18)$$

As deduced from above formulation, to obtain results from the fractal model, the size distribution of contact spots, $n(a)$, must be evaluated, which is the subject of following section.

B.3. Size distribution of contact spots

It has been shown that the cumulative size distribution of the contact spots essentially follows a power law [52]:

$$S(A > a) = \left(\frac{a_l}{a}\right)^{D/2} \quad (19)$$

where S is the total number of contact spots with area larger than a . The distribution is normalized by the area of the largest contact spot (a_l). From the cumulative distribution in Eq. (19), the size distribution of contact spots, $s(a)$, can be obtained by differentiation (Eq. (20)), such that the real area of contact, A_r , can be written as [52]:

$$s(a) = \frac{D}{2} \left(\frac{a_l^{D/2}}{a^{D/2+1}} \right) \quad (20)$$

$$A_r = \int_0^{a_l} s(a) da = \frac{D}{D-1} a_l \quad (21)$$

Finally, the size distribution in Eq. (20) can be used in Eq. (17) to obtain the load-area relation, which can be represented in its non-dimensional form (for the case: $D \neq 1.5$) as [52]:

$$P^* = \frac{4\sqrt{\pi}}{3} G^{*(D-1)} g_1(D) A_r^{*(D/2)} \left[\left(\frac{(2-D)A_r^*}{D} \right)^{(3-2D)/2} - a_c^{*(3-2D)/2} \right] + K\phi g_2(D) A_r^{*(D/2)} a_c^{*(2-D)/2} \quad (22)$$

where

$$g_1(D) = \frac{D}{(3-2D)} \left(\frac{2-D}{D} \right)^{D/2} \quad (23)$$

$$g_2(D) = \frac{D}{(2-D)} \quad (24)$$

and,

$$P^* \frac{P}{A_a E}; \quad G^* = \frac{G}{\sqrt{A_a}}; \quad A_r^* = \frac{A_r}{A_a}; \quad a_c^* = \frac{a_c}{A_a} \quad (25)$$

$$P^* = \sqrt{\pi} G^{*1/2} \left(\frac{A_r^*}{3} \right)^{3/4} \ln \left[\frac{A_r^*}{3a_c^*} \right] + \frac{3K\phi}{4} \left(\frac{A_r^*}{3} \right)^{3/4} a_c^{*1/4} \quad (26)$$

B.4. Surface separation calculation

The compression pressure, p , applied to the fuel cell assembly is known, and given by:

$$p = \frac{P}{A_a} \quad (27)$$

Using the load (P) from Eq. (27), the contact area, A_r , can be evaluated either using Eq. (22) or Eq. (26) depending on the value of the fractal dimension, D . Assuming that the surface heights, $z(x)$, follow a normal probability distribution, the surface mean plane separation (d) can be obtained by the relation [52]:

$$\frac{A_r}{A_a} = \frac{1}{\sqrt{2\pi}} \int_{d/\sigma}^{\infty} e^{-x^2/2} dx = \frac{1}{2} \operatorname{erfc} \left(\frac{d}{\sqrt{2}\sigma} \right) \quad (28)$$

where erfc is the complementary error function. After determining the surface mean plane separation, a digital reconstruction of the BP|DM interface (showing the structure of the interfacial contact) can be created.

B.5. Contact resistance calculation

It has been shown that the contact of two rough surfaces is negligibly different than the contact of a smooth and an equivalent rough surface [45,46]. Such a rough contact produces a large

number of contact spots, with each imposing a certain resistance to the flow of electrons across the surface. This resistance is composed of a series of resistances as a result of small asperities stacked on bigger asperities in a self-similar manner. Since all the contact spots co-exist at the contact plane, these resistances act in parallel, resulting in a series-parallel resistance network. As the number of stacked asperities becomes infinite within the limits of an infinitesimal area, the flow of electrons follows an infinite and extremely complex network of resistances. The complexity of such a network can, however, be reduced by using the fractal nature of the geometry of rough surfaces. The network model developed by Majumdar and Tien [53] uses the feature of self-similarity to reconstruct the network of resistances by repeatedly adding a simple group of resistances in a self-similar pattern. Due to the complex nature of the model, its derivation is omitted from this discussion, however a comprehensive description of the model can be found in Ref. [53]. In this approach, the interfacial contact resistance can be calculated by correlating it to the characteristic fractal parameters (D and G), the material properties of surfaces in contact, and the compression load [53], such as:

$$R = A_a \frac{f(R/\rho)(\rho G^{D-1})}{L^D} \left[\frac{D}{(2-D)A_r^*} \right] \quad (29)$$

where

$$\frac{R}{\rho} = \left[\frac{D(1-A_r^*)}{(2-D)A_r^*} \right]^{1/2} \quad (30)$$

and,

$$f\left(\frac{R}{\rho}\right) = \frac{[1 + \sqrt{1 + 4(R/\rho)}]}{2(R/\rho) + [1 + \sqrt{1 + 4(R/\rho)}]} \quad (31)$$

where L is the characteristic length of the interfacial profile, ρ is the average resistivity of the BP and DM surfaces, and R is the BP|DM contact resistance. Since this approach depends only on the surface profile characteristics and material properties, it can be extended to evaluate the BP|DM interfacial resistance.

References

- [1] M.M. Mench, Fuel Cell Engines, John Wiley & Sons, New York, NY, 2008.
- [2] R. Makharia, M.F. Mathias, D.R. Baker, J. Electrochem. Soc. 152 (2005) A970.
- [3] V. Gurau, T.A. Zawodzinski, J.A. Mann, J. Fuel Cell Sci. Technol. 5 (2008) 021009.
- [4] L. You, H. Liu, Int. J. Heat Mass Transfer 45 (2002) 2277.
- [5] C. Marr, X. Li, J. Power Sources 77 (1999) 17.
- [6] D.M. Bernardi, M.W. Verbrugge, AIChE J. 37 (1991) 1151.
- [7] T.E. Springer, M.S. Wilson, S. Gottesfeld, J. Electrochem. Soc. 140 (1993) 3513.
- [8] R. Roshandel, B. Farhanieh, Int. J. Hydrogen Energy 32 (2007) 4424.
- [9] S. Kamarajugadda, S. Mazumder, J. Power Sources 183 (2008) 629.
- [10] L. You, H. Liu, Int. J. Hydrogen Energy 26 (2001) 991.
- [11] H.M. Yu, C. Ziegler, M. Oszipok, M. Zobel, C. Hebling, Electrochim. Acta 51 (2006) 1199.
- [12] R.P. Ramasamy, E.C. Kumbur, M.M. Mench, W. Liu, D. Moore, M. Murthy, Int. J. Hydrogen Energy 33 (2008) 3351.
- [13] W.M. Yan, C.Y. Hsueh, C.Y. Soong, F. Chen, C.H. Cheng, S.C. Mei, Int. J. Hydrogen Energy 32 (2007) 4452.
- [14] J.H. Nam, K.J. Lee, G.S. Hwang, C.J. Kim, M. Kaviani, Int. J. Heat Mass Transfer 52 (2009) 2779.
- [15] H. Meng, Int. J. Hydrogen Energy 34 (2009) 5488.
- [16] H. Nakajima, T. Konomi, T. Kitahara, J. Power Sources 171 (2007) 457.
- [17] J.H. Nam, M. Kaviani, Int. J. Heat Mass Transfer 46 (2003) 4595.
- [18] A.Z. Weber, J. Newman, J. Electrochem. Soc. 152 (2005) A677.
- [19] Z. Qi, A. Kaufman, J. Power Sources 109 (2002) 38.
- [20] B. Avasarala, P. Haldar, J. Power Sources 188 (2009) 225.
- [21] I. Nitta, O. Himanen, M. Mikkola, Electrochem. Commun. 10 (2008) 47.
- [22] I. Nitta, T. Hottinen, O. Himanen, M. Mikkola, J. Power Sources 171 (2007) 26.
- [23] V. Mishra, F. Yang, R. Pitchumani, ASME J. Fuel Cell Sci. Technol. 1 (2004) 2.
- [24] J. Kleemann, F. Finsterwalder, W. Tillmetz, J. Power Sources 190 (2009) 92.
- [25] L. Zhang, Y. Liu, H. Song, S. Wang, Y. Zhou, S.J. Hu, J. Power Sources 162 (2006) 1165.
- [26] J. Andre, L. Antoni, J.P. Petit, E.D. Vito, A. Montani, Int. J. Hydrogen Energy 34 (2009) 3125.
- [27] S.B. Lee, K.H. Cho, W.G. Lee, H. Jang, J. Power Sources 187 (2009) 318.

- [28] T. Hottinen, O. Himanen, S. Karvonen, I. Nitta, J. Power Sources 171 (2007) 113.
- [29] I. Nitta, S. Karvonen, O. Himanen, M. Mikkola, Fuel Cells (2008) 410.
- [30] P. Zhou, G.J. Wu, G.J. Ma, J. Power Sources 159 (2006) 1115.
- [31] M.H. Akbari, B. Rismanchi, Renew. Energy 33 (2008) 1775.
- [32] X. Lai, D. Liu, L. Peng, J. Ni, J. Power Sources 182 (2008) 153.
- [33] Y. Zhou, G. Lin, A.J. Shih, S.J. Hu, J. Power Sources 163 (2007) 777.
- [34] Z. Wu, S. Wang, L. Zhang, S.J. Hu, J. Power Sources 189 (2009) 1066.
- [35] Z. Wu, Y. Zhou, G. Lin, S. Wang, S.J. Hu, J. Power Sources 182 (2008) 265.
- [36] M. Barber, T.S. Sun, E. Petrach, X. Wang, Q. Zou, J. Power Sources 185 (2008) 1252.
- [37] T. Swamy, E.C. Kumbur, M.M. Mench, J. Electrochem. Soc. 157 (2009) B77.
- [38] F.E. Hızır, S.O. Ural, E.C. Kumbur, M.M. Mench, J. Power Sources 195 (2009) 3463.
- [39] H. Bajpai, M. Khandelwal, E.C. Kumbur, M.M. Mench, J. Power Sources 195 (2010) 4196.
- [40] E.C. Kumbur, K.V. Sharp, M.M. Mench, J. Power Sources 176 (2008) 191.
- [41] J.A. Greenwood, J.W.P. Williamson, Proc. R. Soc. Lond. Ser. A 295 (1966) 300.
- [42] P.R. Nayak, J. Lubric. Technol. 93 (1971) 398.
- [43] J.I. McCool, Wear 107 (1986) 37.
- [44] J.A. Greenwood, Wear 261 (2006) 191.
- [45] A.W. Bush, R.D. Gibson, T.R. Thomas, Wear 35 (1975) 87.
- [46] M. O'Callaghan, M.A. Cameron, Wear 36 (1976) 79.
- [47] M. Ciavarella, V. Delfino, V. Demelio, Wear 261 (2006) 556.
- [48] D. Risović, S.M. Poljaček, M. Gojo, Appl. Surf. Sci. 255 (2009) 4283.
- [49] S. Ganti, B. Bhushan, Wear 180 (1995) 17.
- [50] D. Goerke, K. Willner, Wear 264 (2008) 589.
- [51] A. Majumdar, C.L. Tien, Wear 136 (1990) 313.
- [52] A. Majumdar, B. Bhushan, J. Tribol. 113 (1991) 1.
- [53] A. Majumdar, C.L. Tien, J. Heat Transfer Trans. ASME 113 (1991) 516.
- [54] R. Chopra, F. Podczek, M.J. Newton, G. Alderborn, Part. Syst. Charact. 19 (2002) 277.
- [55] D. Faith, C.J. Horsfield, J. Mater. Sci. 41 (2006) 3973.
- [56] British Standard 1134: Method for the Assessment of Surface Texture, British Standard Institution, London, 1972.
- [57] A. Kusoglu, A.M. Karlsson, M.H. Santare, S. Cleghorn, W.B. Johnson, J. Power Sources 161 (2006) 987.
- [58] S. Kim, M. Khandelwal, C. Chacko, M.M. Mench, J. Electrochem. Soc. 156 (2008) B99.
- [59] A. Turhan, K. Heller, J.S. Brenizer, M.M. Mench, J. Power Sources 160 (2006) 1195.
- [60] Ahmet Turhan, Ph.D. Thesis, Penn State University, 2009.
- [61] A. Turhan, K. Heller, J.S. Brenizer, M.M. Mench, J. Power Sources 180 (2008) 773.
- [62] N. Pekula, K. Heller, P.A. Chuang, A. Turhan, M.M. Mench, J.S. Brenizer, K. Ünlü, Nucl. Instrum. Methods A 542 (2005) 134.
- [63] C. Hartnig, I. Manke, R. Kuhn, N. Kardjilov, J. Banhart, W. Lehnert, Appl. Phys. Lett. 92 (2008) 134106.